Detecting cellular morphological changes through light scattering patterns: comparison of methods

Marina S. Moran[1], Xin-Hua Hu[1], and Jun Q. Lu[1,*]

Abstract: Several methods, including the azimuthally-averaged angular distribution of the scattered light intensity, two bi-parameter scatter plots and three image texture analysis algorithms of the Haralick features, Laws energy measures, and Gabor filters, are compared for their effectiveness in correlating changes in light scattering patterns from biological cells to variations in their morphological features. A series of analytic cell models with variations in main cell structure and mitochondrial characteristics are created to imitate biological cells of different structural attributes. Numerical simulations of light scattering are performed using the discrete dipole approximation (DDA). Our results show that Gabor filter analysis combined with the bi-parameter scatter plots can provide significant insight into cellular morphology.

Keywords: bi-parameter plots, Gabor, Haralick, discrete dipole approximation.

1. Introduction

The light scattering pattern from biological cells contains rich information regarding the cell structure and its optical properties. Due to the complexity of the internal structure of the cell, the light scattering pattern formed through the interference of the scattering wavefields from various components in the cell is rather complicated, and no simple relation can be established between individual speckles in the scattering pattern and particular components of the cell[1]. Most of the previous cell light scattering pattern analysis focuses on the azimuthally-averaged angular distribution of the scattered light intensity, where only the cell size and some limited information regarding the internal structure of the cell can be obtained[2–6]. The other often-employed method is the bi-parameter scatter plot of forward-scatter intensity versus side-scatter intensity, a technique regularly used in flow cytometry to distinguish between various subpopulations of cells[7]. More recent studies have attempted to analyze the diffraction images of cells to extract additional intracellular information utilizing a variety of methods. The Haralick features, Laws energy measures, and speckle analysis methods have been used to differentiate between perinuclear, diffuse, peripheral, and/or aggregate mitochondrial distributions within a cell[8,9]. While these results have shown promise of quantitative discrimination of cells based on various morphological characteristics, these methods have only been applied to simplified cell models with spherically-shaped cells and mitochondria. In addition, the above-mentioned methods were not capable of detecting variations in a range of cell properties such as the number and volume density of mitochondria[9].

In this study, we compare the effectiveness of several analysis methods in analyzing light scattering patterns from realistic biological cell models. In addition to the above-mentioned Haralick features, Laws energy measures, the angular distribution of the scattered light intensity, and the bi-parameter scatter plot, we introduce the Gabor filter technique to the application of analyzing light scattering patterns. Gabor filters have proved very useful for texture classification and image recognition and have recently been utilized to quantify dynamic changes in the mitochondrial structure of apoptotic cells[10–12]. To evaluate the capabilities of these methods, we

[1]Department of Physics, East Carolina University, Greenville, NC 27858, USA.

[*]Corresponding Author: Jun Q. Lu. Email: luj@ecu.edu.

systematically alter the structure of a cell model to determine how well each method can detect the corresponding changes in the light scattering patterns. The cell structural variations introduced comprise of cell shape and surface fluctuation, nucleus size, and mitochondrial characteristics (shape, spatial distribution, and volume density). Our results suggest that two bi-parameter plots combined with the Gabor filter approach provide substantial information regarding the major structural features and mitochondrial properties of the cell.

2. Methods

2.1. Realistic analytic cell modeling and light scattering simulation

Analytic cell models are used in this report for a controlled study relating cell components to features in light scattering patterns. The analytic cell model consists of two parts: the main cell structure, which consists of the nucleus and cell membrane, and the mitochondria. The shapes of real biological cells and their nuclei are nonspherical in general with various degrees of surface fluctuations. We have recently developed a procedure[13] to model a realistic cell structure by taking these factors into consideration. In this method, each of the cell and nucleus shapes is modeled as a smooth base shape, and the random surface fluctuations are implemented though a Gaussian Random Sphere (G-sphere) method[14]. In the G-sphere method adopted here, the surface fluctuations are specified by two parameters: the relative standard deviation (σ) and the exponent (ν) of a power law expansion of the log-radius covariance function of the surface. The former describes the degree of deformation of the surface from a perfect sphere while the latter is associated with the number of hills and valleys per solid angle. The code developed by Nousiainen and McFarquhar is used to generate the G-spheres[14]. For the realistic cell models used in this report, the base shapes of the cell and nucleus are both assumed to be ellipsoids and all of the parameters for the base shapes and surface fluctuations are extracted from z-stacks of confocal microscopic images of NALM-6 pre-B cells[15].

The characteristics of mitochondria in a cell, such as spatial distribution, volume density, shape and size, are reported to be closely related to the metabolic activity in the cell[16–19]. Changes in spatial distribution and density have been linked to a number of cell physiological processes and diseases; for example, a perinuclear aggregation of mitochondria has been associated with normal cells, while a diffuse distribution has been found in cancer cells[19,20]. To simulate realistic cells, the mitochondria in the cell models used in this study vary in shape and size, ranging from equal-sized spheres to smooth ellipsoids of various sizes and axis ratios, and are distributed randomly in the cytoplasm according to specific configurations. The detailed information for each case studied is presented in the results section below.

Light scattering patterns from the cell models are calculated using the Discrete Dipole Approximation (DDA) method, a sophisticated numerical method to solve for the scattered field from an arbitrarily-shaped scatterer[21]. This method approximates the scatterer as a finite array of points, which acquire dipole moments in response to the incident electric field and their mutual interactions. The C implementation of the DDA method developed by Yurkin and Hoekstra[21], ADDA, is adapted for this study. Here the scatterer is divided into a 3D grid of small cells with resolution specified by the number of dipoles per wavelength (dpl), and the structure of the cell is realized numerically by assigning proper values of the index of refraction to each grid point. The desired output is the Mueller matrix as a function of the scattering angle θ_s and the azimuthal angle ϕ_s and the scattering or diffraction images can be obtained by projecting the S_{11} element of the Mueller matrix in designated directions.

2.2. Image analysis methods

As discussed in the introduction, three image texture analysis methods, the Haralick features, Laws energy measures, and Gabor filters are applied to analyze the projected images.

The Haralick texture features provide information such as homogeneity, contrast, and structure of the image[1]. Fourteen features can be derived from co-occurrence matrices, which describe the frequencies of certain gray tones appearing in a specified spatial relationship in an image. For an image of n gray tone values, the co-occurrence matrix is a nxn matrix whose values P_{ij} stand for the number of times a pixel with value i is found within a certain distance d to a pixel with value j. The distance between pixels can be defined horizontally, vertically, or diagonally (in two directions), resulting in four co-occurrence matrices that can be computed for a specified distance between pixels[22]. To examine the small-scale texture features and avoid averaging over several textures in an image, the co-occurrence matrix is often computed using a moving window around each pixel. In this study, a moving window of size 15x15 pixels is chosen and the gray levels of the images are quantized to eight values, as common in the literature[23]. Results presented in the section below are obtained from the co-occurrence matrix calculated for nearest neighbors (d=1) and averaged over the four orientations. Furthermore, only 11 out of the 14 Haralick features are calculated due to computational difficulties in features #12-13 and instability in #14.

The Laws energy measures have various functions, such as detecting edges, spots, and ripples in an image. These measures are derived from a set of independent, two-dimensional filter masks obtained by convolutions of specific vectors of order 3, 5, or 7. For example, the "Edge" vector of order 5, E5, convoluted with the "Spot" vector of the same order, S5, produces the so-called E5S5 mask, which is sensitive to textures with low correlation[24]. Convoluting the vectors of order 5 with each other yields a set of 25 masks, which are often normalized by the first mask, resulting in a set of 24 masks. In this study, an image is filtered using each mask, and the absolute value in local neighborhoods (15x15 pixels) around each pixel of the filtered image is summed to yield a set of 24 texture energy images. The arithmetic mean of these images yields a set of 24 energy measures for each original image.

A Gabor filter is a sinusoidal mask of a specific frequency and orientation modulated by a Gaussian envelope. The general practice is to apply a set of filters with different frequencies and orientations to a given image to examine its texture features[25]. Based on the characteristics of the scattering images from the cell models used in this study, three frequencies (0.1, 0.2 and 0.4 per pixel) and four orientations evenly spaced from 0° to 135° are chosen to construct a set of 3x4 Gabor filters. The size of the filter is set to be 21x21 pixels. By applying this set of filters to the projected scattering images of the cell models, a set of 3x4 Gabor-filtered images is produced for each image. The code developed by Manjunath[11] is used here for the calculations. For quantitative comparison purposes, the arithmetic mean of each Gabor-filtered image is computed, and as a result, each scattering image is represented by a set of twelve numbers when analyzed in this manner. The notation G_{mn} represents the arithmetic mean of the Gabor-filtered image produced by applying the filter with the m^{th} frequency and n^{th} orientation to an image. For example, G_{33} represents the arithmetic mean of the Gabor-filtered image produced by applying the filter with frequency 0.4 cycles per pixel and orientation 90° to an image.

Each of the three texture analysis methods described above yields a feature vector consisting of a set of values that represents a scattering image. To find an accurate and efficient way to differentiate images using these vectors, we explored the combinations of the vector components that would best characterize each scattering image when plotted in a scatter plot. For the various cases studied in the section below, the best combinations were found to be Difference Variance vs. Sum Average for the Haralick features, *S5R5* vs. *E5W5*, a convolution of the Spot and Ripple vectors versus that of the Edge and Wave vectors, for Laws measures, and G_{33} vs. G_{13} for the Gabor measures. These combinations are displayed in scatter plots which are referred to as Haralick, Laws, or Gabor scatter plots below.

3. Results and discussion

In this section, we compare the capabilities of the analysis techniques discussed earlier in

differentiating light scattering patterns obtained from cell models with various cell and mitochondrial characteristics.

To this end, we created a series of analytic cell models with the desired structure features. These cell models are divided into five groups based on their basic structure, ranging from the simplest to the more realistic one, by gradually introducing realistic features into the cell structure. Group #1 consists of the simplest cell models where the basic cell structure is approximated by a concentric spherical nucleus and cell. In group #2, the basic cell structure is modeled by an off-centered, ellipsoid-shaped nucleus and cell. The cell structure in group #2 is improved upon with the introduction of surface fluctuation for both the nucleus and cell in group #3. In these three groups, the mitochondria population is approximated by equal-sized spheres. Further improvement of the cell structure results in group #4 with the introduction of size variation among the spherical mitochondria. In group #5, the spherically-shaped mitochondria in group #4 are replaced by ellipsoidal mitochondria with various sizes and axis ratios.

The radii of the spherical nucleus and cell of the models in group #1 measure 2.55 and 5.03μm to match the nucleus and cell volumes of the models in other groups. The axial lengths of the ellipsoidal base shapes of the cell models in group #2 to #5 are taken to be 5.13, 4.58 and 5.33μm for the cell and 2.83, 2.10, and 2.63μm for the nucleus. This size configuration produces a volume ratio of nucleus to cell of approximately 12.5%. The parameters for the surface fluctuations are set to be ν= 4.2 and σ= 0.0814 for the cell and ν= 3.1 and σ = 0.0963 for the nucleus. An extra small-scale fluctuation is also added to the cell base shape to provide finer surface roughness with ν = 2.0 and σ= 0.03.

Within each of the cell groups described above, the mitochondria are placed in the cytoplasm according to a specific combination of spatial distribution and volume density. Three distributions are selected for this study: the diffuse (homogeneously spread out in the cytoplasm), the peripheral (close to the membrane), and the perinuclear (close to the nucleus)[9]. The dimensions of the peripheral and perinuclear zones, limited by the size range and density of the mitochondria, are set to be 0.8μm along the radius direction. The mitochondrial density, defined as ratio of the total volume of the mitochondria to that of the cell, is chosen to be 1.0, 4.0 and 7.0%. Here the number of mitochondria is allowed to vary among the three densities since the individual mitochondrial size range is fixed. The radii of the spherical mitochondria in cell groups #1 to #3 vary slightly among cell models with different densities and distributions in the range of 0.29μm – 0.31μm in order to keep the number of mitochondria similar among different distributions. The radius range of the spherical mitochondria of various sizes in model #4 is 0.19μm - 0.42μm. The axial lengths for the ellipsoidal mitochondria in model #5 are adopted from the literature[18,19] with the major axis in the range 0.3μm - 0.8μm and the minor axes in the range 0.15μm - 0.3μm. The size variation introduced in cell groups #4 and #5 generate some relatively larger mitochondria. These larger mitochondria, few in numbers, pose some degree of difficulty in fitting a similar number of mitochondria in all distributions. In particular, due to the limited zone size in the perinuclear distribution, a larger number of smaller mitochondria are needed to reach the required density for the cases of 4.0 and 7.0%.

With three spatial distributions and three densities for mitochondria in each of the five basic structure groups, a total of forty-five analytic cell models are created. The Mueller matrix as a function of the scattering angle (θ_s) and the azimuthal angle (ϕ_s) is calculated using the DDA method for each of the cell models for eight incident orientations spanning evenly in space. For all of the calculations, the dpl in the DDA method is set at 10 and the wavelength at 1.0μm. The index of refraction of the cytoplasm is assumed to be 1.3675, and that of the nucleus and mitochondria to be 1.4 and 1.42, respectively, at this wavelength. The cell is assumed to be immersed inside a host medium of index of refraction 1.35.

For image texture analysis purposes, the scattering patterns of the cell models are obtained by projecting the S_{11} element of the Mueller matrix onto a plane at a distance of 500μm with

$\theta_s = 90^\circ \pm 30^\circ$ and $\phi_s = 90^\circ \pm 30^\circ$ to mimic experimental flow cytometer acquisition of the scattering signal[26,27]. With angular resolution of 1° along each direction, this produces a projected scattering image of size 61x61 pixels. Examples of the cell models in groups #1 and #5 with perinuclear, diffuse, and peripheral mitochondrial distributions and their corresponding projected scattering images are shown in Fig. 1. The mitochondrial density is 4.0% for these cell models. It is clear that the projected images are very different among cell models with different structure characteristics; the intensity evens out more in the field of view as the cell models become more complicated and the speckle size decreases as the mitochondrial distribution moves closer to the membrane.

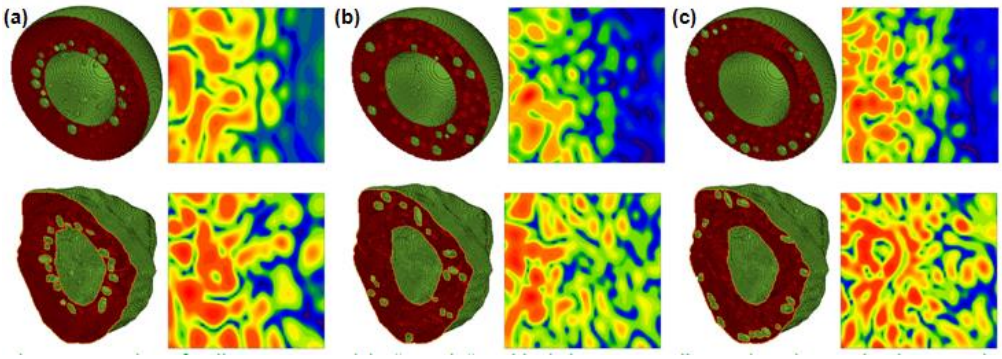

Fig. 1. Examples of cell models and their corresponding projected scattering images. Top: concentric spherical cell model with equal-sized spherical mitochondria in cell group #1; Bottom: realistic cell model with ellipsoidal base shape, surface fluctuation, and varying-sized ellipsoidal mitochondria in cell group #5. Models are shown with (a) perinuclear, (b) diffuse, and (c) peripheral mitochondrial distributions.

For an initial analysis of the light scattering data, we first plot the azimuthally-averaged angular distribution of the scattered light intensity, the S_{11} element of the Mueller matrix, averaged over the eight incident orientations for the entire scattering angle range of 0° - 180°. Results for cell groups #1 - #3 and #4 - #5 are displayed in Fig. 2(a) and (b), respectively, with each of the forty-five cell models presented by one curve. In this figure and the ones following (Figs. 3-6), the results for cell models with different mitochondrial spatial distributions are represented by blue (diffuse), red (peripheral), and green (perinuclear) symbols, and the mitochondrial densities are indicated by the shade of the color, from light (1%) to dark (7%).

The curves with the large oscillations in Fig. 2(a) are those of the cell models in group #1 due to spherical symmetry in the main cell structure. Since all of the models have the same cell and nucleus volume, all of the curves overlap very well in the first 10° when plotted together, demonstrating the well-known fact that the forward scattering is closely related to the cell volume and cell scattering power, and it also shows that the forward scattering is not very sensitive to cell structure variation. Beyond 10°, the curves group differently in separate regions of the scattering angle. From 10° to 50°, the curves appear to group according to mitochondrial spatial distribution with the perinuclear distribution well separated from the other two distributions. From 40° to 100°, the curves group according to mitochondrial density, and the curves for cell models with density 1% are better separated from the others. This density-based grouping extends to the rest of the plot in Fig. 2(b) and reappears in the larger scattering angle region in Fig. 2(a). In the region from 80° to 140°, the curves group according to their basic structure. The curves in Fig. 2(a) are significantly lower in this region with a dip at 110° while those in Fig. 2(b) are relatively leveled in this region. Closer examination of Fig. 2(b) shows that the curves for cell models in

structure groups #4 and #5 are well separated in this region.

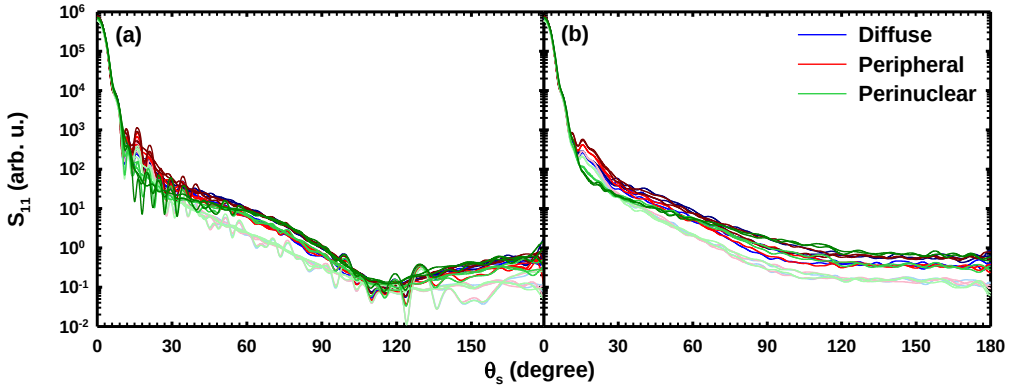

Fig. 2. The azimuthally-averaged angular distribution of the scattered light intensity averaged over the eight incident orientations. (a) Results of cell models in groups #1 - #3; (b) Results of cell models in groups #4 - #5. Mitochondrial density is indicated by the shade of the color, from light (1%) to dark (7%).

With these observations in mind, we explore different ways of differentiating the cell models utilizing data from various scattering angle regions in Fig. 2. It is found that the bi-parameter scatter plot of the forward scatter ($S_{11}(0°)$) versus the integral of S_{11} over the range θ_s= 25° - 45° or θ_s= 90° - 110° is very effective in detecting most of the changes in cell structure, and the results are presented in Figs. 3(a) and (b), respectively. Note that, instead of the orientation-averaged data in Fig. 2, data for the eight individual orientations of each cell model are displayed here, with each orientation represented by a data point. Data for cell models of the five different basic structure groups are plotted in ascending order from group #1 to group #5 in both Fig. 3(a) and (b) for detailed analysis.

The bi-parameter scatter plot of $S_{11}(0°)$ vs. $\int_{90°}^{110°} S_{11}(\theta_s)d\theta_s$ in Fig. 3(a) clearly shows that data points for each cell model respond strongly to changes in the structure. The plot for cell group #1 contains three distinct sub-groups corresponding to the three mitochondrial densities (increasing from left to right) and within each sub-group, the spatial distributions of the mitochondria can be separated by the forward scatter intensity. As the complexity of the cell base shape increases in cell groups #2 and #3, the gaps between the sub-groups decrease and the data points spread out vertically. The scatter plot undergoes more dramatic changes when mitochondria size variations are introduced from cell group #3 to #4 and alters even more when mitochondria shapes are modeled as ellipsoids in group #5, manifested by the visible horizontal shift to the right of the mitochondria density sub-groups from cell groups #3 to #5 and the larger and better-defined separation between sub-groups of different densities. These results indicate that this type of scatter plot is very sensitive to the changes in the individual mitochondrion. It is noteworthy that the data points in the plot of cell group #4

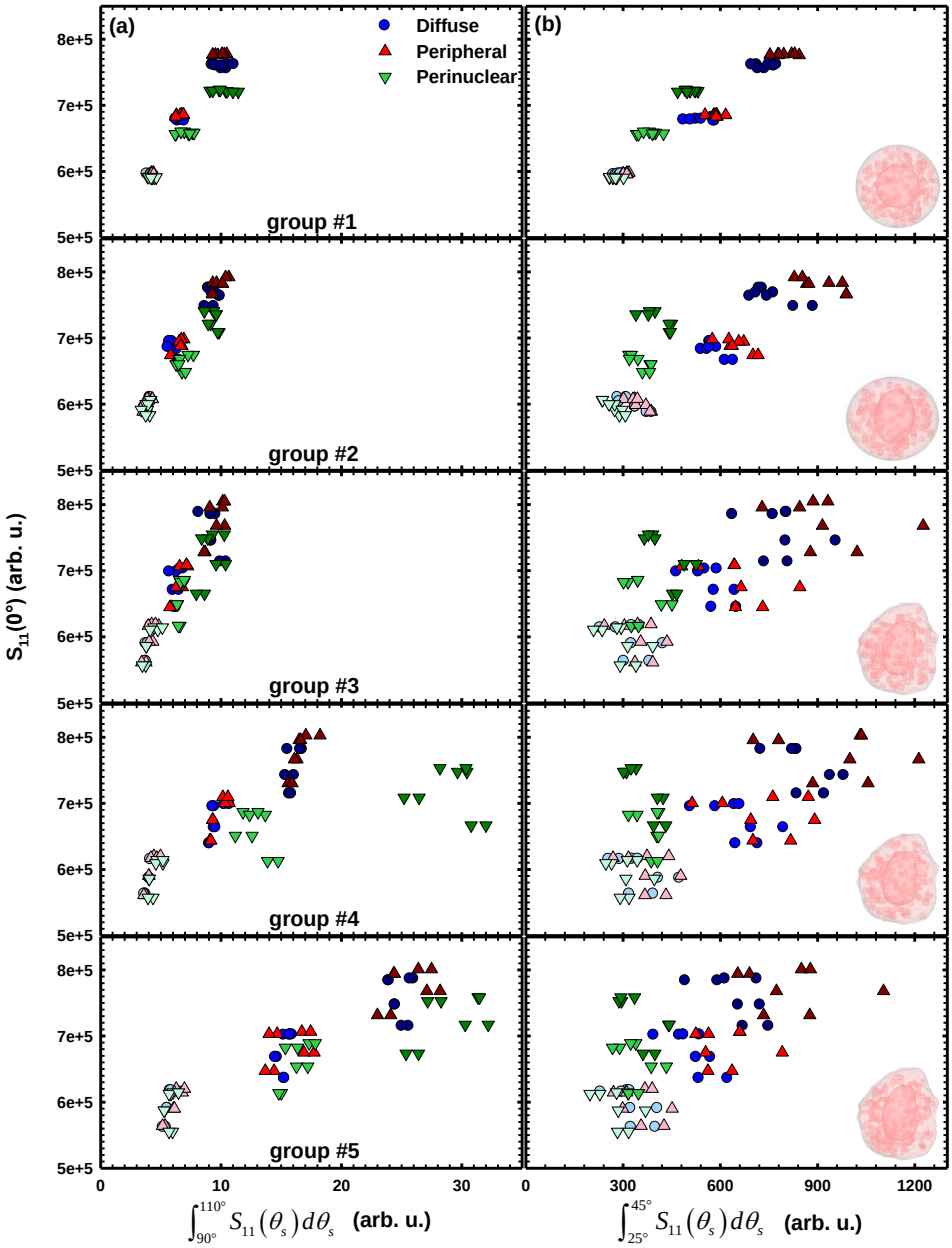

Fig. 3. Bi-parameter scatter plots of the forward intensity versus the azimuthally-averaged intensity integrated over the scattering angle range of (a) 90°–110° (left panel) and (b) 25°–45° (right panel). Results of all eight incident orientations for each cell model are present. Data of cell models in groups #1–#5 are plotted separately from top to bottom. Mitochondrial density is indicated by the shade of the color, from light (1%) to dark (7%). The inserts are examples of the cell models in each cell group.

Corresponding to the two cell models with larger mitochondrial densities and a perinuclear distribution shifted far more to the right than the data points of other cell models in the corresponding density sub-groups. Further tests show that this out-of-group behavior is caused by the aforementioned, relatively larger number of smaller mitochondria used for these cell models, a consequence of space limitation in the perinuclear zone for spherically-shaped mitochondria. The space limitation issue is not as severe in the case of cell group #5 when the

shape is replaced by ellipsoids, thus no such effects are observed in the plot for cell group #5. This effect, though undesired, further demonstrates the capability of this type of bi-parameter scatter plot in detecting variation within the mitochondrial population for fixed mitochondrial density.

A different grouping pattern of data points and different response to cell structural changes are observed in Fig. 3(b), the bi-parameter scatter plot of $S_{11}(0°)$ vs. $\int_{25°}^{45°} S_{11}(\theta_s)d\theta_s$. While clear subgroups of different mitochondrial densities and spatial distributions can be recognized in the plot for cell group #1, the gaps between those subgroups quickly disappear when the base shape of the cell models changes from cell group #1 to #3, especially in cell group #3 where the surface fluctuations are introduced. As modifications are made to the size and shape of the mitochondria in cell groups #4 and 5, however, no significant changes are observed. On the other hand, even though the signal in this region seems not sensitive to the characteristics of individual mitochondrion, one can recognize to a certain extent the perinuclear distribution in each of the five models. This implies that the signal in this angular range is most sensitive to changes in the overall structure rather than individual mitochondrial changes.

In summary, the azimuthally-averaged angular distribution of the scattered light intensity provides valuable insight into the structure of the cell model. Signals in different angular regions provide information about different aspects of the cell structure: the forward scattering region for the cell size, 25° - 45° for the main cell structure, and 90° - 110° for individual mitochondrial characteristics. Although it has been suggested that the forward scatter can differentiate between mitochondrial spatial distributions[28], as reaffirmed in the scatter plot of group #1 in Fig. 3, the distinction between distributions is less evident in the plots of groups #2 - #5. This also demonstrates the necessity of using realistic cell models for quantitative studies of optical cell structure using light scattering signals.

Next, we analyze the projected scattering images using the image analysis methods described in the previous section. The images are first analyzed by the Gabor filter method, and the arithmetic means G_{33} and G_{13} of the Gabor-filtered images are computed for each orientation of the cell models to create the Gabor scatter plots of G_{33} vs. G_{13}. Unlike the data in Fig. 3, the Gabor scatter plot does not seem to be sensitive to main cell structure changes, with the data points spread out in a similar range for all five basic structure groups, although slightly more packed in cell groups #4 and #5. Due to the lack of significant differences between the results of the groups, the data for all forty-five models is shown together in one plot in Fig. 4. We note that the data points of the cell models with the same mitochondrial

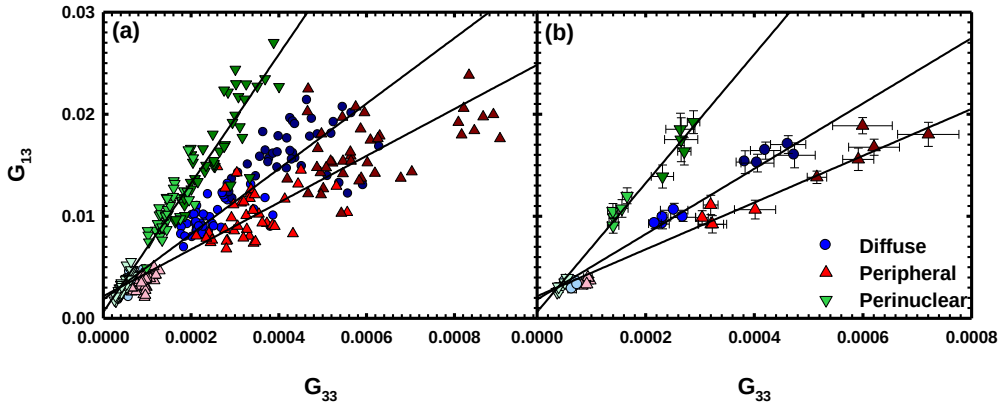

Fig. 4. Gabor scatter plot with data from all cell models in groups #1 - #5. (a) Results with all eight incident orientations for each cell model; (b) Results averaged over the eight incident orientations (±1 standard deviation). Mitochondrial spatial distributions are distinguished by

different lines of best fit. Mitochondrial density is indicated by the shade of the color, from light (1%) to dark (7%).

distribution but different in other structure characterization lie approximately along a line, and that the slope of the line is different for different distribution types. This pattern is much clearer in Fig. 4(b), where the data are averaged over the eight individual orientations for each cell model. The best-fit line of each distribution type has a significantly different slope, with 63.1, 32.0, and 22.9 for perinuclear, diffuse, and peripheral, respectively. This feature indicates that the Gabor scatter plot may provide a quantitative way of differentiating cells with different mitochondrial distributions. In additional to the distribution separation, Fig. 4, especially Fig. 4(b), also separates very well the data points for cell models with different mitochondrial densities.

We then analyze the same set of images using Haralick and Laws methods. Similar to the case of Gabor scatter plots, there are no significant changes between the scatter plots of cell models associated with different structure groups. For this reason, only results for cell group #5 are shown in Fig. 5 with the corresponding scatter plots for Haralick and Laws in Fig. 5(a) and (b), respectively. The data points are closely packed in both cases, and there is a significant amount of overlapping among groups corresponding to different mitochondrial distributions and densities, especially in the Haralick plot. However, the perinuclear distribution in the Laws plot is well separated, agreeing with the results from previous studies[5]. It is evident that these two methods are not as effective as the bi-parameter S_{11} scatter plot in Fig. 3 and Gabor scatter plot in Fig. 4 in distinguishing between mitochondrial characteristics in realistic models.

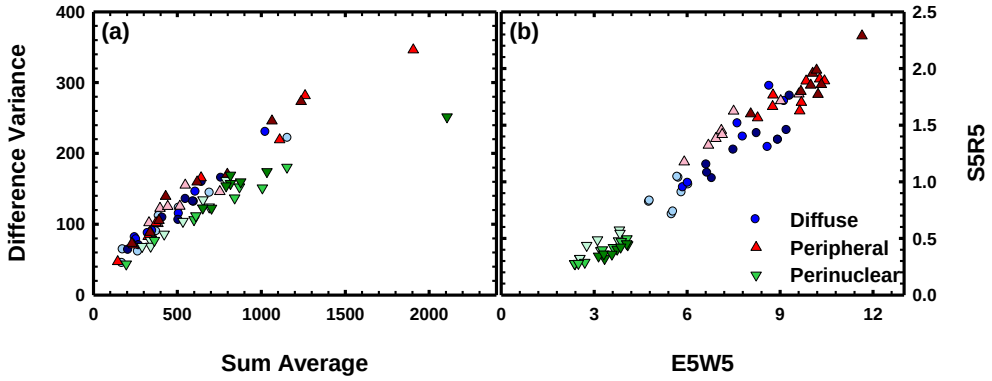

Fig. 5. (a) Haralick and (b) Laws scatter plots for cell models in group #5. Mitochondrial density is indicated by the shade of the color, from light (1%) to dark (7%).

We would like to point out that scatter plots using several other pairs of Law energy measures, such as R5E5 and W5E5, can separate the data points of cell models with a perinuclear mitochondrial distribution from those with the other distributions when the simplest basic structure model #1 is used. However, such advantage disappears once the basic structure of the cell becomes more complicated as the structure changes from group #1 to #5. This information further indicates the need for a realistic cell model for the development of accurate cell scattering image analysis techniques.

In the last part of this study, we compare the ability of the methods in detecting differences in nuclear size in the cell models, a parameter that varies greatly among cell types. Here the nucleus volume of cell group #5 is increased from 12.5% of the total cell volume to 25.0% and 50.0%. A larger nucleus reduces the available space for the mitochondria in the cytoplasm; consequently, the cell models are limited to diffuse mitochondrial distribution only for the 50.0% case. Results for cell models in group #5 are presented in the form of the bi-parameter scatter plot of the

forward scatter versus the integral of S_{11} over the range θ_s=90° - 110° in Fig. 6(a) and the Gabor scatter plot in Fig. 6(b). The results in both plots in Fig. 6 are orientation-averaged. The effect of nucleus size is most evident in Fig. 6(a) as greater nucleus volume increases forward scatter. The points are well grouped vertically according to nuclear size and horizontally according to density, and the points are closely packed within each group. The Gabor scatter plot in Fig. 6(b), similar to Fig. 4, is responsive to mitochondrial distribution, but is less dependent on nucleus volume size, with only a slight shift to the right with increase in nucleus size. The latter behavior further confirms the observation discussed earlier that the Gabor scatter plot for images at this scattering angle is not very sensitive to changes in the cell's main structure.

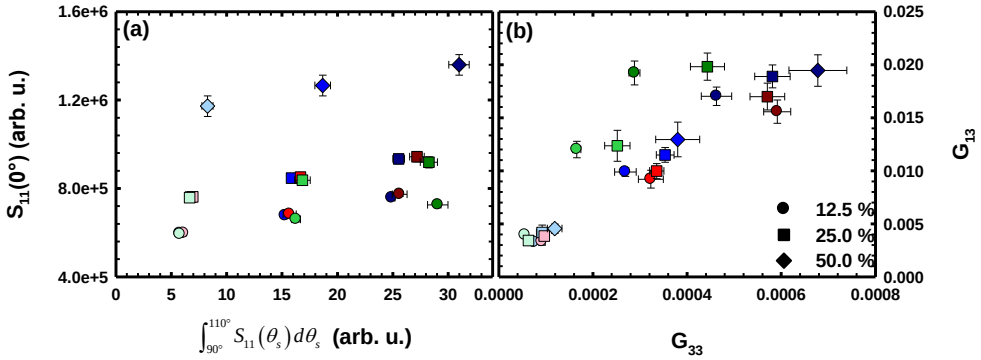

Fig. 6. Comparison of cell models with different nucleus-to-cell volume ratios. Only the realistic cell models from group #5 are used. (a) The forward intensity versus the azimuthally-averaged intensity integrated over the scattering angle range of 90°–110°; (b) Gabor scatter plot. The data in each plot is averaged over the eight incident orientations (±1 standard deviation). Mitochondrial spatial distributions are represented by blue (diffuse), red (peripheral), and green (perinuclear) color, and the shade of each color indicates mitochondrial densities, from light (1%) to dark (7%).

4. Conclusion

In this work we investigated the capabilities of various analysis methods in correlating alternations in cell models to changes alternations in the light scattering patterns. We gradually increased the complexity of the cell model, starting from the standard spherical cell model with spherical mitochondria to an off-centered ellipsoidal base shape with surface fluctuation and ellipsoidal mitochondria of various sizes. The influence of these structural variations on light scattering patterns was examined through analysis with the bi-parameter plots, and the Gabor, Haralick, and Laws image texture analysis methods. It was found that the bi-parameter plots responded strongly to an increase in the complexity of the cell model, and they have the ability to identify changes in the cell's main structure as well as in individual mitochondrial characterization in the population. In particular, the bi-parameter plot of S_{11} with an angular range of 90° - 110° is well suited for characterization of mitochondrial density and nucleus size. This level of sensitivity to intracellular structure in the bi-parameter scatter plots of S_{11} demonstrates the need for realistic cell modeling in light scattering studies. The results of texture analysis on diffraction images show that the Laws and Haralick texture measures are not very efficient in discriminating structure variations in realistic cell models, while the Gabor scatter plot, however, has the potential to provide a new and quantitative approach to distinguish different mitochondrial distributions. Improvement of a quantitative approach for analysis of diffraction images is underway to extend these methods to the study of human blood cells for clinical applications.

Acknowledgement: M. Moran would like to thank Dr. R. S. Brock for his generous support on many computing related aspects of this project. This work was supported in part by a NIH grant (2R15GM70798-02).

References:

1. **K. Dong, Y. Feng, K. M. Jacobs, J. Q. Lu, et al.**, "Label-free classification of cultured cells through diffraction imaging," Biomed. Opt. Express **2**(6), 1717 (2011).
2. **H. Ding, J. Q. Lu, R. S. Brock, T. J. McConnell, et al.**, "Angle-resolved Mueller matrix study of light scattering by B-cells at three wavelengths of 442, 633, and 850 nm," J. Biomed. Opt. **12**(3), 34032 (2007).
3. **J. Zhang, Y. Feng, W. Jiang, J. Q. Lu, et al.**, "Realistic optical cell modeling and diffraction imaging simulation for study of optical and morphological parameters of nucleus," Opt. Express **24**(1), 366 (2016).
4. **C. Li, S. R. Grobmyer, L. Chen, Q. Zhang, et al.**, "Multispectral diffuse optical tomography with absorption and scattering spectral constraints.," Appl. Opt. **46**(34), 8229–8236 (2007).
5. **L. Zhang, D. K. Pleskow, V. Turzhitsky, E. U. Yee, et al.**, "Light scattering spectroscopy identifies the malignant potential of pancreatic cysts during endoscopy," Nat. Biomed. Eng. **1**(4), 40 (2017).
6. **H. F. Zhang, K. Maslov, G. Stoica, and L. V Wang**, "Functional photoacoustic microscopy for high-resolution and noninvasive in vivo imaging," Nat. Biotechnol. **24**(7), 848–851 (2006).
7. **H. M. Shapiro**, *Practical Flow Cytometry*, Wiley-Liss (2003).
8. **X. Su, S. Liu, X. Qiao, Y. Yang, et al.**, "Pattern recognition cytometry for label-free cell classification by 2D light scattering measurements," Opt. Express **23(**21), 27558 (2015).
9. **P. M. Pilarski, X.-T. Su, D. M. Glerum, and C. J. Backhouse**, "Computational analysis of mitochondrial placement and aggregation effects on wide-angle cell scattering patterns," Proc. SPIE, Vol. 7187, id. 71870J (2009). **7187**, A. Wax and V. Backman, Eds., 71870J–71870J–12 (2009).
10. **R. M. Pasternack, B. Rabin, J.-Y. Zheng, and N. N. Boustany**, "Quantifying subcellular dynamics in apoptotic cells with two-dimensional Gabor filters.," Biomed. Opt. Express **1**(2), 720–728 (2010).
11. **B. S. Manjunath**, "Texture features for browsing and retrieval of image data," IEEE Trans. Pattern Anal. Mach. Intell. **18**(8), 837–842 (1996).
12. **J. G. Daugman**, "Complete Discrete 2-D Gabor Transforms by Neural Networks for Image Analysis and Compression," IEEE Trans. Acoust. **36**(7), 1169–1179 (1988).
13. **M. Moran, X.-H. Hu, and J. Q. Lu**, "Correlating the light scattering pattern of a biological cell to its mitochondrial properties using a Gabor filter technique," A. P. Wax and V. Backman, Eds., 1–8 (2012).
14. **T. Nousiainen, G. M. McFarquhar, T. Nousiainen, and G. M. McFarquhar**, "Light Scattering by Quasi-Spherical Ice Crystals," J. Atmos. Sci. **61**(18), 2229–2248 (2004).
15. **J. Yoon, K. Kim, H. Park, C. Choi, et al.**, "Label-free characterization of white blood cells by measuring 3D refractive index maps," Biomed. Opt. Express **6**(10), 3865 (2015).
16. **Q. Yu and A. A. Heikal**, "Two-photon autofluorescence dynamics imaging reveals sensitivity of intracellular NADH concentration and conformation to cell physiology at the single-cell level," J. Photochem. Photobiol. B Biol. **95**(1), 46–57 (2009).

17. **S. Zhai and H. Zhao**, "Enhancement of Sensitivity of the Solution-Phase Localized Surface Plasmon by a Nanostructured Substrate," MRS Adv. **1**(28), 2059–2064 (2016).

18. **J. S. Modica-Napolitano and K. K. Singh**, "Mitochondria as targets for detection and treatment of cancer.," Expert Rev. Mol. Med. **4**(9), 1–19 (2002).

19. **P. L. Gourley, J. K. Hendricks, A. E. McDonald, R. G. Copeland, et al.**, "Ultrafast nanolaser flow device for detecting cancer in single cells.," Biomed. Microdevices **7**(4), 331–339 (2005).

20. **T. J. Collins, M. J. Berridge, P. Lipp, and M. D. Bootman**, "Mitochondria are morphologically and functionally heterogeneous within cells," EMBO J. **21**(7), 1616–1627 (2002).

21. **M. A. Yurkin, V. P. Maltsev, and A. G. Hoekstra**, "The discrete dipole approximation for simulation of light scattering by particles much larger than the wavelength," J. Quant. Spectrosc. Radiat. Transf. **106**(1–3), 546–557 (2007).

22. **R. M. Haralick, K. Shanmugam, and I. Dinstein**, "Textural Features for Image Classification," IEEE Trans. Syst. Man. Cybern. **SMC-3**(6), 610–621 (1973).

23. **D. A. Clausi**, "An analysis of co-occurrence texture statistics as a function of grey level quantization," Can. J. Remote Sens. **28**(1), 45–62 (2002).

24. **M. Tuceryan and A. K. Jain**, "Texture analysis," in Handbook of Pattern Recognition and Computer Vision, pp. 235–276 (1993).

25. **L. C. L. Chen, G. L. G. Lu, and D. Z. D. Zhang**, "Effects of different Gabor filters parameters on image retrieval by texture," 10th Int. Multimed. Model. Conf. 2004. Proceedings., 0–5 (2004).

26. **K. M. Jacobs, J. Q. Lu, and X.-H. Hu**, "Development of a diffraction imaging flow cytometer.," Opt. Lett. **34**(19), 2985–2987 (2009).

27. **K. M. Jacobs, L. V. Yang, J. Ding, A. E. Ekpenyong, et al.**, "Diffraction imaging of spheres and melanoma cells with a microscope objective," J. Biophotonics **2**(8–9), 521–527 (2009).

28. **X. Lin, N. Wan, L. Weng, and Y. Zhou**, "Angular-dependent light scattering from cancer cells in different phases of the cell cycle," Appl. Opt. **56**(29), 8154 (2017).

